

# Electronic structure of epitaxial anatase TiO<sub>2</sub> films: Angle-resolved photoelectron spectroscopy study

Masato Emori,<sup>1</sup> Mari Sugita,<sup>1</sup> Kenichi Ozawa,<sup>2</sup> and Hiroshi Sakama<sup>1,\*</sup>

<sup>1</sup>*Department of Physics, Sophia University, Kioi-cho, Chiyoda-ku, Tokyo 102-8554, Japan*

<sup>2</sup>*Department of Chemistry and Materials Science, Tokyo Institute of Technology, Ookayama, Meguro-ku, Tokyo 152-8551, Japan*

(Received 14 May 2011; revised manuscript received 31 October 2011; published 31 January 2012)

Synchrotron-radiation angle-resolved photoelectron spectroscopy has been utilized to examine the bulk valence-band structure of anatase TiO<sub>2</sub>(001) thin films fabricated on LaAlO<sub>3</sub>(100) by pulsed laser deposition. The energy-momentum dispersion relation of O 2*p*-derived nonbonding, O 2*p*-Ti 3*d*  $\sigma$  bonding and several  $\pi$  bonding states is determined experimentally. The nonbonding state at the top of the valence band is located at 4.3 eV at the center of the bulk Brillouin zone, and it shifts towards the shallower energies to 3.8 eV at the zone boundary. No other states with binding energies smaller than 3.8 eV are found on any other high-symmetry axes and points. Thus the valence-band maximum is located at the zone boundary. Our finding proves that anatase is an indirect-band-gap semiconductor.

DOI: [10.1103/PhysRevB.85.035129](https://doi.org/10.1103/PhysRevB.85.035129)

PACS number(s): 79.60.Dp

## I. INTRODUCTION

Photocatalytic degradation of toxic organic compounds in water, soil, and air in the presence of photocatalytic materials has received much attention over the past two decades.<sup>1-5</sup> Photocatalytic activity is due to a photoexcited electron in the conduction band and a hole left behind in the valence band. Electrons and holes are a good reductant and a powerful oxidant, respectively, and they can initiate redox reactions on the catalyst surface.<sup>2</sup> Of all materials that exhibit photocatalytic activity, titanium dioxide (TiO<sub>2</sub>) is most promising because of its high efficiency, chemical stability, nontoxicity, and low cost of production.<sup>5</sup>

TiO<sub>2</sub> exists in nature as minerals in three different polymorphs; rutile, anatase, and brookite. There have been many studies on the electronic and structural properties of TiO<sub>2</sub>, especially the rutile polymorph. Rutile is an important rock-forming mineral and the most abundant TiO<sub>2</sub> polymorph in nature. However, less abundant anatase has attracted much attention as a photocatalyst because of its efficiency superior to that of rutile.<sup>6-8</sup> Basic properties of anatase have been investigated, and some fundamental aspects relating to their photocatalytic activity such as the behavior of excitons have been revealed.<sup>9-11</sup> Nevertheless, some important issues remain unanswered.

One of the controversial issues is whether anatase TiO<sub>2</sub> has a direct band gap or an indirect band gap. Many theoretical studies have been carried out to elucidate the band structure of anatase.<sup>12-20</sup> The theoretical investigations have all shown that the conduction-band minimum (CBM) is located at the center of the bulk Brillouin zone (BZ).<sup>12-20</sup> However, the position of the valence-band maximum (VBM) depends on the calculation methods employed. The study using a full potential linearized augmented plane-wave (FLAPW) method by Asahi *et al.* predicts the VBM position at the  $\Gamma$  point.<sup>13</sup> This result suggests that anatase has a direct band gap at the zone center. On the other hand, the orthogonalized linear-combinations-of-atomic-orbitals method by Mo and Chiang<sup>12</sup> as well as several density-functional theory (DFT) calculations<sup>14-19</sup> show that the VBM should be near the zone

boundary. Another DFT study by Hitosugi *et al.* also gives the band with the VBM at the off- $\Gamma$  point, but near the zone center.<sup>20</sup> These latter results imply that anatase is an indirect-band-gap material.

For a better understanding of the transport property of photogenerated electrons and holes and of the electron-hole recombination process, which directly affect the photocatalytic activity, it is crucial to determine the band-gap type of anatase TiO<sub>2</sub>, i.e., the VBM position. However, no experimental investigation has been attempted to directly examine the valence-band structure of anatase. The lack of the experimental investigation results from the fact that anatase is thermodynamically unstable in comparison with rutile,<sup>21,22</sup> so that large-scale single crystals have not been easily obtained. Fortunately, recent thin-film fabrication techniques allow us to prepare single-crystal anatase thin films on substrates such as SrTiO<sub>3</sub>(100) and LaAlO<sub>3</sub>(100).<sup>23-26</sup> On these oxide substrates, the anatase TiO<sub>2</sub> film is grown with (001) orientation. Because of a small lattice mismatch between anatase TiO<sub>2</sub>(001) and LaAlO<sub>3</sub>(100) (0.1%) in comparison with SrTiO<sub>3</sub>(100) (3.1%), the anatase thin film is obtained with a better crystallinity on LaAlO<sub>3</sub>(100) than on SrTiO<sub>3</sub>(100).<sup>27</sup>

In the present study, single-crystal anatase TiO<sub>2</sub> films were prepared on LaAlO<sub>3</sub>(100) by pulsed laser deposition (PLD), and the valence electronic structure was investigated by angle-resolved photoelectron spectroscopy (ARPES) utilizing synchrotron radiation. The bulk band structure of anatase was determined in great detail. Special attention was paid to the position of the VBM in the bulk BZ. We have found that the experimental band structure is in good agreement with theoretical band structure with the VBM off the center of the bulk BZ.

## II. EXPERIMENT

Single-crystal anatase TiO<sub>2</sub>(001) thin films were grown using PLD with a KrF excimer laser ( $\lambda = 248$  nm) on LaAlO<sub>3</sub>(100). PLD was conducted at a substrate temperature of 970 K and an O<sub>2</sub> pressure of 1.0 Pa. Details on the growth procedure is found in the literature.<sup>26</sup> The x-ray-diffraction (XRD) pattern of the TiO<sub>2</sub> film showed (004) and (008)

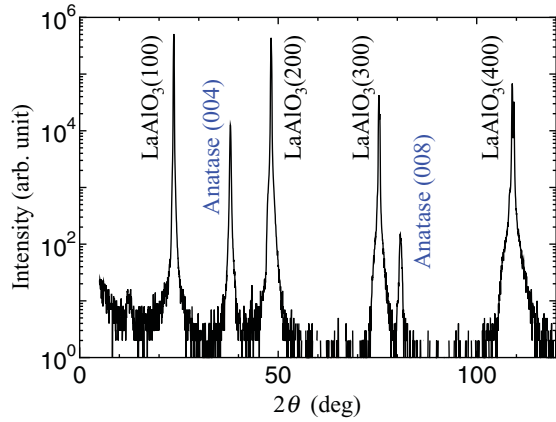


FIG. 1. (Color) XRD pattern of  $\text{TiO}_2$  thin film of  $0.5\text{-}\mu\text{m}$  thickness deposited on  $\text{LaAlO}_3(100)$ .  $\text{Cu-K}\alpha$  x-ray source was used for radiation.

reflections from the anatase phase in addition to substrate reflections as shown in Fig. 1, indicating that (001) oriented anatase was indeed obtained. Since no other peaks were observed, crystallinity of the anatase film was high. The azimuthal direction of the film was checked by reflection high-energy electron diffraction. The (001)-oriented anatase films were epitaxially grown with a relationship of [100] anatase//[010]  $\text{LaAlO}_3$ .

The anatase  $\text{TiO}_2$  sample was fixed on a Ta holder and was inserted into the ultrahigh vacuum chamber with a base pressure of  $2.0 \times 10^{-8}$  Pa. The *in situ* preparation to remove surface contamination involved cycles of  $\text{Ar}^+$  sputtering (2.5 kV,  $0.5 \mu\text{A}$ ) and annealing at 900 K for several times. The sample was then annealed at 700 K in  $\text{O}_2$  atmosphere ( $1.0 \times 10^{-4}$  Pa) for 5 min to restore the surface stoichiometry. The surface thus prepared showed a  $(4 \times 1)$  low-energy electron-diffraction pattern, a typical reconstruction structure for the anatase (001) surface.<sup>28</sup> The work function of the clean surfaces, determined from the photon energy and the width of photoelectron spectra from the Fermi level to the secondary electron cutoff, was 5.4 eV. The value is in good agreement with literature values of anatase  $\text{TiO}_2(001)$ .<sup>29–31</sup>

The ARPES measurements were performed utilizing synchrotron radiation at beamline 3B of the Photon Factory, High Energy Accelerator Research Organization (KEK). A sector-type hemispherical electron energy analyzer (HA45, VSW) was used to acquire the spectra with a typical overall energy resolution of 0.2 eV at the photon energy of 60 eV. The incidence light was linearly polarized within the incidence plane, which was set parallel to the detection plane of the photoelectrons. The measurements were conducted at room temperature. Since both  $\text{TiO}_2$  and  $\text{LaAlO}_3$  are semiconductors, sample charging was expected during the photoemission measurements. We confirmed absence of sample charging by varying the incident photon flux. This implies a certain amount of oxygen vacancies in the bulk. Nevertheless, as we will see below, the low concentration of the oxygen vacancies was achieved in the surface region.

Anatase  $\text{TiO}_2$  has a body-centered-tetragonal (bct) structure ( $I4_1/amd$  space group) [Fig. 2(a)] with lattice constants of  $a = 0.379$  nm and  $c = 0.951$  nm.<sup>32</sup> The bulk BZ for the

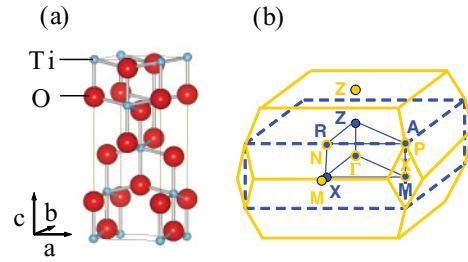


FIG. 2. (Color) Bulk atomic structure (a) and the bulk Brillouin zone (BZ) (b) of anatase  $\text{TiO}_2$ . The BZs for the body-centered-tetragonal structure (thick solid lines) and for the simple tetragonal structure (dashed lines) are indicated.

bct structure is depicted in Fig. 2(b). Among the theoretical band calculation studies, some employed the BZ for the bct structure,<sup>14,15,18,19</sup> while others examined the band structure assuming the BZ for the simple tetragonal structure.<sup>12,13,16,17,20</sup> The BZ for the simple tetragonal structure is shown by dashed lines in Fig. 2(b). In the present ARPES study, we examined the band structure along the high-symmetry axes of the BZ for the simple tetragonal structure, i.e., the  $\Gamma$ -X, Z-R,  $\Gamma$ -Z,  $\Gamma$ -M, and Z-A axes, which corresponds to the  $\Gamma$ -M-Z, Z/2-N,  $\Gamma$ -Z,  $\Gamma$ -X and Z/2-P axes of the BZ for the bct structure. To examine the band structure at a certain wave number in the bulk BZ, i.e.,  $k = (k_{\parallel}, k_{\perp})$ , a spectrum was measured at a set of a photon energy ( $h\nu$ ) and a detection angle of the photoelectrons ( $\theta_d$ ) determined by the following equations:

$$k_{\parallel} = \hbar^{-1} \sqrt{2m^*(h\nu - \phi - E_{\text{bin}})} \sin \theta_d, \quad (1)$$

$$k_{\perp} = \hbar^{-1} \sqrt{2m^*\{(h\nu - \phi - E_{\text{bin}}) \cos^2 \theta_d + V_0\}}. \quad (2)$$

$k_{\parallel}$  and  $k_{\perp}$  are the wave numbers parallel and perpendicular to the (001) plane ( $ab$  plane), respectively.  $\phi$  is the work function, and the measured value of 5.4 eV was used.  $V_0$  is an inner potential, which was determined to be  $16 (\pm 1)$  eV from the value of  $\phi$  (5.4 eV) and the bottom position of the valence band (9–11 eV below  $E_F$ ). The effective mass of an electron ( $m^*$ ) was determined so that maxima and minima of branches of the valence bands coincide with the high-symmetry points of the extended bulk BZ. The value of  $m^*$  was  $(0.88 \pm 0.01)m_e$ , where  $m_e$  was the rest mass of an electron.

The electronic structure on the  $\Gamma$ -Z axis was determined from a series of the normal emission spectra measured at  $h\nu$  between 45 and 80 eV, which covers the  $\Gamma$ -Z axis from the 10th to the 14th BZ ( $32 < k_{\perp} < 44 \text{ nm}^{-1}$ ). For the band structures on the  $\Gamma$ -X and Z-R axes (the  $\Gamma$ -M-Z and Z/2-N axes, respectively, for the bct notation), the detection plane was set parallel to the [100] direction, and the spectra were acquired at  $(h\nu, \theta_d)$  from  $(64.3 \text{ eV}, 0.0^\circ)$  to  $(91.4 \text{ eV}, 35.3^\circ)$  for  $\Gamma$ -X and from  $(76.2 \text{ eV}, 0.0^\circ)$  to  $(101 \text{ eV}, 33.0^\circ)$  for Z-R. With the detection plane parallel to the [110] direction, a series of spectra measured at  $(h\nu, \theta_d)$  ranging from  $(64.3 \text{ eV}, 0.0^\circ)$  to  $(118 \text{ eV}, 45.5^\circ)$  and from  $(74.7 \text{ eV}, 0.0^\circ)$  to  $(128 \text{ eV}, 42.6^\circ)$  gave the band structures on the  $\Gamma$ -M and Z-R axes (the  $\Gamma$ -X and Z/2-P axes for bct), respectively.

The electron binding energy of the spectra presented in the paper is referenced to the Fermi energy ( $E_F$ ), which was

determined from the Fermi cutoff in the spectra of the Ta sample holder.

### III. RESULTS AND DISCUSSION

Figure 3 shows ARPES spectra along the selected high-symmetry axes of the bulk BZ. The valence band of TiO<sub>2</sub>, composed of the O 2*p* states with a minor contribution of the Ti 3*d* states,<sup>33,34</sup> is observed between 4 and 10 eV. In the band-gap region, only a very weak emission is seen at 1 eV below the Fermi level, where the Ti 3*d* states are expected if the TiO<sub>2</sub> surface is reduced and the Ti<sup>3+</sup> species are formed.<sup>35</sup> Thus the concentration of the O vacancies is low on the anatase TiO<sub>2</sub>(001)-(4×1) surface prepared in the present study, in good agreement with the photoemission study by Thomas *et al.*<sup>34</sup> Of all emission peaks observed, none of them is associated with the surface-localized states, because the peaks are not sensitive to adsorption of contaminants such as water in the analysis chamber.

The valence-band spectra are characterized by two intense peaks at the upper and lower binding energy regions and weak emission structures in between them. These features have already been identified by the recent photoemission studies.<sup>33,34</sup> On the basis of the FLAPW calculations by Asahi *et al.*,<sup>13</sup> the valence band is decomposed into roughly three contributions: the O 2*p*-derived  $P_\pi$  nonbonding states in the upper valence-band region, the O 2*p*- and Ti  $t_{2g}$ -derived  $\pi$  bonding states in the middle energy region, and the  $\sigma$  bonding states formed by the Ti  $e_g$  and O 2*p* <sub>$\sigma$</sub>  states in the lower region. Figure 3 shows that some of the emission peaks show substantial energy shift depending on both  $h\nu$  and  $\theta_d$ , reflecting energy dispersion of the valence states along the high-symmetry axes of the bulk BZ.

To clarify energy dispersion of the valence states, grayscale band maps are constructed by plotting spectral weight of the second derivatives of the measured ARPES spectra. Figure 4

shows the grayscale band maps along the selected axes of the bulk BZ. The  $P_\pi$  nonbonding and  $\sigma$  bonding states are observed as bright bands at the upper (4–5 eV) and lower (7–9 eV) parts of the valence-band region, respectively, and the  $\pi$  bonding states are seen at 5–7 eV. These bands exhibit quite complex dispersion structures. However, a close examination reveals that some of the bands have clear periodic dispersion; for example, the top  $P_\pi$  band on the  $\Gamma$ - $M$  axis ( $\Gamma$ - $X$  for bct) shows local maxima and minima in energy at the  $M$  ( $X$ ) points and the  $\Gamma$  points, respectively. Similarly, the  $P_\pi$  band on  $Z$ - $A$  ( $Z/2$ - $P$  for bct) also shows local maxima and minima at  $A$  ( $P$  for bct) and  $Z$  ( $Z/2$  for bct), respectively. Regarding the  $\sigma$  band at the bottom of the valence region, periodic structures are recognized on the  $\Gamma$ - $X$ ,  $\Gamma$ - $M$ , and  $Z$ - $A$  axes ( $\Gamma$ - $M$ - $Z$ ,  $\Gamma$ - $X$ ,  $Z/2$ - $P$  for bct, respectively).

For more quantitative information on the band structure, each valence-band spectrum is decomposed into components by least-squares fitting using Gaussian functions and a linear function. In the fitting procedure, a linear function is assumed for the background of the spectrum, and three or four Gaussian functions are used to reproduce the background-subtracted spectrum. The height, the width, and the position of each Gaussian are treated as variables. We first start least-squares fitting with three Gaussians, and the fourth Gaussian is added if the peak width of one of the Gaussian peaks is much larger, typically more than three times, in comparison with the other two peaks. A part of the results are shown in the bottom spectra in Fig. 3. The shallowest peaks at  $E_{\text{bin}} = 4$ –5 eV are associated with the O 2*p*-derived  $P_\pi$  nonbonding states, while the contribution from the  $\sigma$  bonding states gives the peaks at  $E_{\text{bin}} = 7$ –9 eV.<sup>13</sup> In the energy region between the  $P_\pi$  and  $\sigma$  states,  $\pi$  bonding states are resolved including the second shallowest peak with a relatively large intensity at around 5 eV.<sup>36</sup>

Plots of the binding energies of the resolved components against  $k$  give the bulk valence-band structure of anatase TiO<sub>2</sub> as shown in Fig. 5. Each plotted point corresponds to

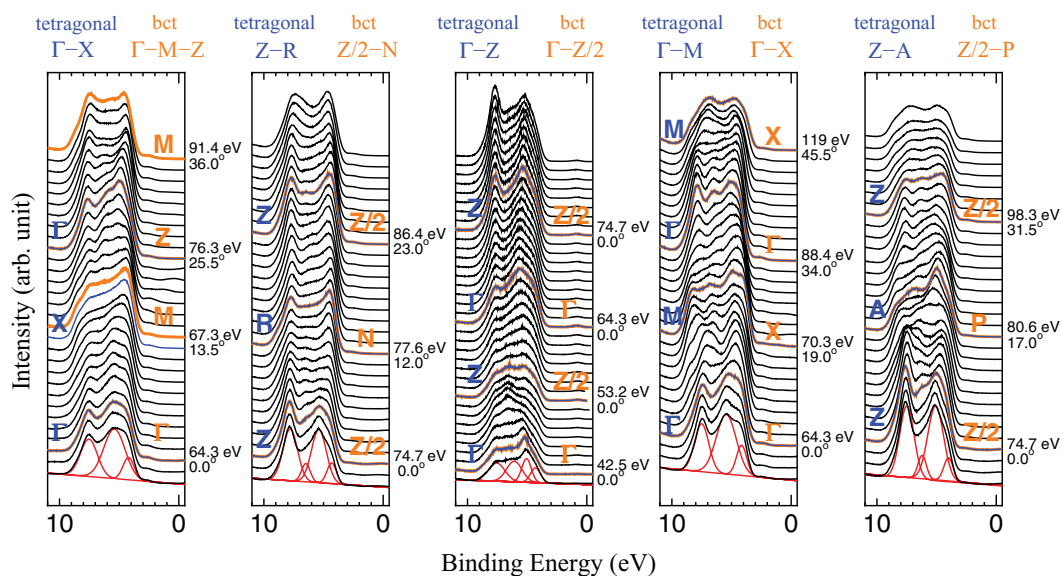


FIG. 3. (Color) ARPES spectra of the anatase TiO<sub>2</sub> thin films along the selected axes of the bulk BZ. Both  $h\nu$  and  $\theta_d$  were adjusted to acquire the spectra along the selected points on the axes. The values used for the spectra at the high-symmetry points are indicated. Results of least-square fitting using Gaussian functions and a linear function are shown in the bottom spectra.

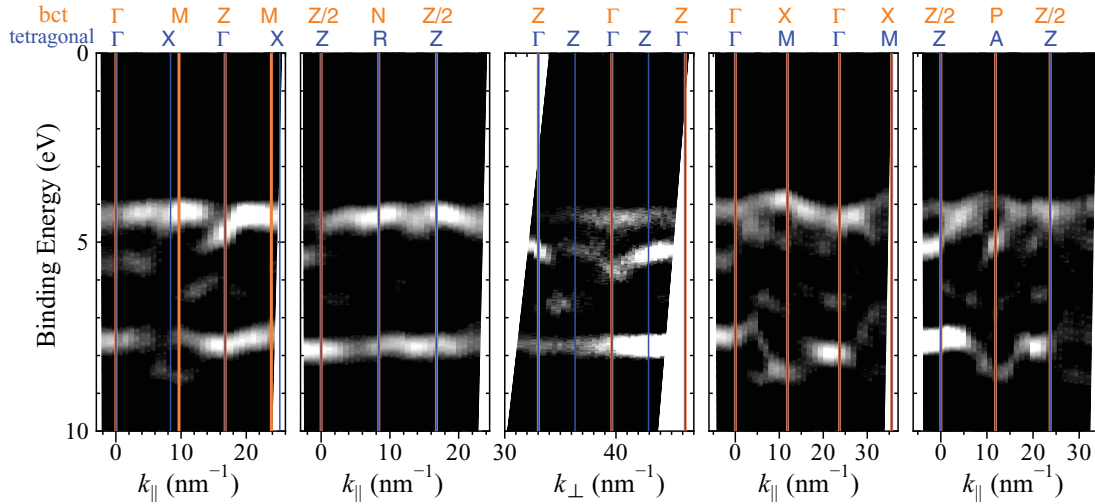


FIG. 4. (Color) Intensity plots of the second derivatives of the measured spectra shown in Fig. 3. Bright and dark regions correspond to the high and low spectral weight regions, respectively.

the position of the Gaussian peak, and the size of the point represents the integrated intensity of the peak. The  $P_\pi$  state forms an almost flat band at 4.3 eV on  $\Gamma$ -X ( $\Gamma$ -M-Z for bct) and Z-R (Z/2-N for bct), while the state moves to the shallower energies from 4.3 eV at  $\Gamma$  to 3.8 eV at M (X for bct) and from 4.3 eV at Z (Z/2 for bct) to 4.1 eV at A (P for bct).

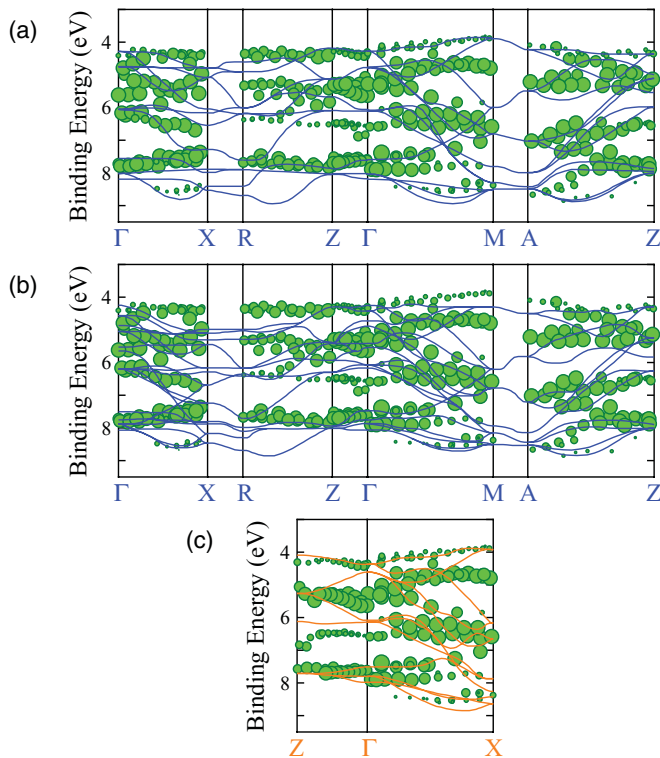


FIG. 5. (Color) Comparison of the experimental band (indicated by circles, whose size represents the emission intensity) with the theoretical bands (solid lines). Theoretical bands are obtained by (a) the hybrid DFT calculations by Zhang *et al.* (Ref. 17), (b) the FLAPW calculations by Asahi *et al.* (Ref. 13), and (c) the DFT calculations by Mikami *et al.* (Ref. 14).

No other states with binding energies smaller than 3.8 eV are found in any other high-symmetry axes and points. This fact is more clearly indicated in Fig. 6, in which the spectrum at the M point (the X point for bct) is compared with those at other high-symmetry points. Thus the  $P_\pi$  state at the M point (the X point for bct) should correspond to the VBM.

In Fig. 5, we compared the experimentally determined band structure with the theoretical bands. Solid lines in Fig. 5(a) and 5(b) are the results of the hybrid DFT calculations by Zhang *et al.*<sup>17</sup> and the FLAPW calculations by Asahi *et al.*,<sup>13</sup> both of which employ the BZ for the simple tetragonal structure. The energy position of the calculated band is aligned so that the state at the  $\Gamma$  point coincides with the experimental value of 4.3 eV. Moreover, the energy widths of the calculated valence bands are diminished to 94% for the hybrid DFT and 90% for the FLAPW to align with the bottom of the experimental

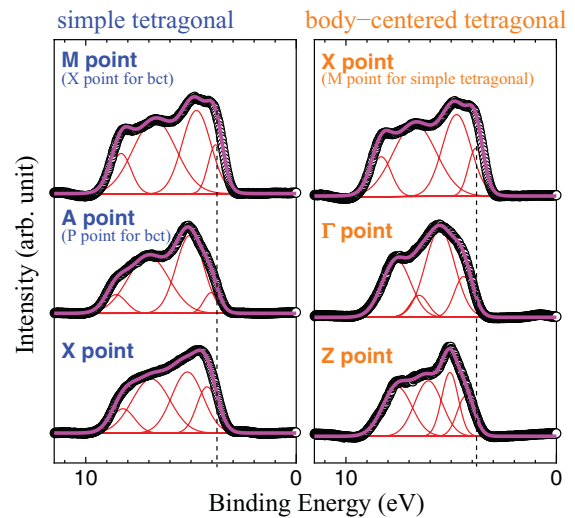


FIG. 6. (Color online) Comparison of the spectrum at the M point (the X point for bct) with those at other high-symmetry points of the bulk BZ. The results of the least-squares fitting are shown by solid lines. Details of fitting are given in the text.

valence band, which appears at 8.8 eV at a  $k$  point on the  $Z$ - $A$  axis.

The dispersion width of the top  $P_\pi$  band on  $\Gamma$ - $M$  and  $A$ - $Z$  is in good agreement between the experiment and the hybrid DFT band, while the theoretical band does not reproduce the  $P_\pi$  band on  $\Gamma$ - $X$  and  $R$ - $Z$  [Fig. 5(a)]. Regarding the FLAPW result, the overall agreement with the experimental band is rather poor for the  $P_\pi$  band on all axes [Fig. 5(b)]. In the lower part of the valence-band region, comparison of the experimental bands with theoretical bands reveals that the  $\sigma$  band at 7.5–8 eV with the high emission intensity is assigned to the flat bands just above the bottom of the valence band, while the band at 8–9 eV, which has a low emission intensity, should correspond to the bottom edge of the dispersing bands. In the  $\pi$  band region, the number of the experimentally resolved bands is apparently smaller than the number of the theoretical bands. This is due to the limitation of the experimental energy resolution as well as the weak emission intensity of the  $\pi$  states in comparison with the  $P_\pi$  and  $\sigma$  states. Nevertheless, we see that some parts of the experimental bands can be associated with the theoretical bands.

Figure 5(c) shows the comparison with the DFT band by Mikami *et al.*<sup>14</sup> along the  $\Gamma$ - $Z$  and  $\Gamma$ - $X$  axes (the bct notation). Although the reproducibility of the  $\pi$  band in the middle part of the valence region is again poor, correspondence between the experiment and the theory is satisfactory for the  $P_\pi$  and  $\sigma$  bands. Band dispersion from  $\Gamma$  to the VBM at the  $X$  point is especially well reproduced.

The most important result of the present study is that the VBM position is determined experimentally. Although many theoretical studies have predicted that the VBM of anatase TiO<sub>2</sub> is at the point close to the  $M$  point (the  $X$  point for bct),<sup>12,14–19</sup> some exceptions have also been reported.<sup>13,20</sup> Experimentally, the VBM is found at the  $M$  point (the  $X$  point for bct). Unfortunately, we cannot say whether the VBM is located *at M* ( $X$ ) or *near M* ( $X$ ). However, our finding decisively indicates that anatase TiO<sub>2</sub> has an indirect band gap. Thus the present study has solved the conflicting theoretical results for the band-gap type of anatase TiO<sub>2</sub>.

Among the major polymorphs of TiO<sub>2</sub>, i.e., rutile, anatase, and brookite, only anatase has the indirect band gap, whereas both rutile and brookite have the direct band gap at the  $\Gamma$  point.<sup>12,16</sup> The indirect band gap in anatase should affect the behavior of photoexcited electrons and holes. Time-resolved photoluminescence measurements have revealed that photoexcited electrons and holes are relaxed nonradiatively to the CBM and VBM, respectively, form self-trapped excitons (STEs) and are finally quenched by radiative recombination at low temperatures (10 K).<sup>37,38</sup> In contrast, those in rutile form free excitons. At room temperature, on the other hand, the formation of STEs is suppressed and the nonradiative recombination through an overlap of the excited state and ground state of electrons dominates the relaxation process

in anatase.<sup>39</sup> Time-resolved transient absorption spectroscopy (TRTAS) has been utilized to investigate the relaxation process of photoexcited electrons and holes in anatase and rutile nanocrystals at room temperature.<sup>40</sup> The decay curve of transient absorption at a fixed wavelength as a function of delay time was fitted by exponential decay components. The resultant time constants are in  $\mu$ s range for both anatase and rutile and these long decay times in anatase and rutile are associated with electrons trapped at surface defect sites (oxygen vacancies).<sup>41</sup> These decay channels at surface dominate the relaxation dynamics in nanocrystals at room temperature, irrespective of crystal structures.

Recently, the recombination rate constant of electron and hole in single-crystal rutile has been evaluated to be  $5 \times 10^{-13} \text{ cm}^{-3} \text{ s}^{-1}$  using TRTAS, which is much smaller than the diffusion rate constant of these carriers ( $1.4 \times 10^{-8} \text{ cm}^{-3} \text{ s}^{-1}$ ).<sup>42</sup> This demonstrates that photoexcited electrons and holes in bulk TiO<sub>2</sub> suffer from direct recombination immediately after their relaxation to the CBM and VBM. However, the direct recombination requires the absorption or emission of phonons in anatase, whereas does not in rutile, as mentioned above. Therefore the reactivity of photoexcited electrons and holes should be lower in anatase than in rutile. Very recently, the decay of time-resolved transient photoconductance spectrum has been shown to be much slower in anatase (>10 ns) than that in rutile (<1 ns).<sup>43</sup> The band-gap type (direct or indirect) plays an important role in the recombination rate, i.e., lifetime of electrons and holes. The lifetime of photogenerated carriers is closely related to the photocatalytic activity.<sup>37,38</sup> The superiority of the photocatalytic activity of the anatase form over the rutile form is owing partly to the valence-band structure with the indirect band gap.

#### IV. SUMMARY

Angle-resolved photoelectron spectroscopy is utilized to determine the valence-band structure of single-crystal anatase TiO<sub>2</sub> films fabricated on LaAlO<sub>3</sub>(100). The O  $P_\pi$  nonbonding state and O  $2p$ -Ti  $e_g$ -derived  $\sigma$  bonding state form band with energy dispersion at the upper and lower parts of the valence-band region. Several O  $2p$ -Ti  $t_{2g}$ -derived  $\pi$  bonding bands are also identified between the  $P_\pi$  and  $\sigma$  bands. These valence bands are observed in the binding-energy region between 3.8 and 8.8 eV with the shallowest state at the  $M$  point for the simple tetragonal (the  $X$  point for the bct). Since the CBM of anatase is located at the center of the bulk BZ, anatase is classified as an indirect-band-gap semiconductor.

#### ACKNOWLEDGMENTS

The ARPES measurements were performed under the approval of the Photon Factory Advisory Committee (Proposals No. 2006G026 and No. 2009G573).

\*h-sakama@sophia.ac.jp

<sup>1</sup>M. A. Fox and M. T. Dulay, *Chem. Rev.* **93**, 341 (1993).

<sup>2</sup>A. L. Linsebigler, G. Lu, and J. T. Yates, *Chem. Rev.* **95**, 735 (1995).

<sup>3</sup>J. H. Carey, J. Lawrence, and H. M. Tosine, *Bull. Environ. Contam. Toxicol.* **16**, 697 (1976).

<sup>4</sup>J. C. Yu, J. Lin, and R. W. Kwok, *J. Photochem. Photobiol. A* **111**, 199 (1997).

- <sup>5</sup>B. O'regan and M. Grätzel, *Nature (London)* **353**, 737 (1991).
- <sup>6</sup>A. Fujishima and K. Honda, *Nature (London)* **238**, 37 (1972).
- <sup>7</sup>M. Grätzel, *Comments Inorg. Chem.* **12**, 93 (1991).
- <sup>8</sup>K. I. Hadjiivanov and D. G. Klissurski, *Chem. Soc. Rev.* **25**, 61 (1996).
- <sup>9</sup>H. Tang, H. Berger, P. E. Schmid, F. Lévy, and G. Burry, *Solid State Commun.* **87**, 847 (1993).
- <sup>10</sup>H. Tang, F. Lévy, H. Berger, and P. E. Schmid, *Phys. Rev. B* **52**, 7771 (1995).
- <sup>11</sup>K. Wakabayashi, Y. Yamaguchi, T. Sekiya, and S. Kurita, *J. Lumin.* **112**, 50 (2005).
- <sup>12</sup>S.-D. Mo and W. Y. Ching, *Phys. Rev. B* **51**, 13023 (1995).
- <sup>13</sup>R. Asahi, Y. Taga, W. Mannstadt, and A. J. Freeman, *Phys. Rev. B* **61**, 7459 (2000).
- <sup>14</sup>M. Mikami, S. Nakamura, O. Kitao, H. Arakawa, and X. Gonze, *Jpn. J. Appl. Phys.* **39**, L847 (2000).
- <sup>15</sup>M. Calatayud, P. Mori-Sánchez, A. Beltrán, A. M. Pendás, E. Francisco, J. Andrés, and J. M. Recio, *Phys. Rev. B* **64**, 184113 (2001).
- <sup>16</sup>M.-Y. Kuo, C.-L. Chen, C.-Y. Hua, H.-C. Yang, and P. Shen, *J. Phys. Chem. B* **109**, 8693 (2005).
- <sup>17</sup>Y.-F. Zhang, W. Lin, Y. Li, K.-N. Ding, and J.-Q. Li, *J. Phys. Chem. B* **109**, 19270 (2005).
- <sup>18</sup>L. Thulin and J. Guerra, *Phys. Rev. B* **77**, 195112 (2008).
- <sup>19</sup>L. Chiodo, J. M. García-Lastra, A. Iacomino, S. Ossicini, J. Zhao, H. Petek, and A. Rubio, *Phys. Rev. B* **82**, 045207 (2010).
- <sup>20</sup>T. Hitosugi, H. Kamisaka, K. Yamashita, H. Nogawa, Y. Furubayashi, S. Nakao, N. Yamada, A. Chikamatsu, H. Kumigashira, M. Oshima, Y. Hirose, T. Shimada, and T. Hasegawa, *Appl. Phys. Express* **1**, 111203 (2008).
- <sup>21</sup>C. Suresh, V. Biju, P. Mukundan, and K. G. K. Warriier, *Polyhedron* **17**, 3131 (1998).
- <sup>22</sup>D.-J. Won, C.-H. Wang, H.-K. Jang, and D.-J. Choi, *Appl. Phys. A* **73**, 595 (2001).
- <sup>23</sup>S. Chen, M. G. Mason, H. J. Gysling, G. R. Paz-Pujalt, T. N. Blanton, T. Castro, K. M. Chen, C. P. Fictorie, W. L. Gladfelter, A. Franciosi, P. I. Cohen, and J. F. Evans, *J. Vac. Sci. Technol. A* **11**, 2419 (2009).
- <sup>24</sup>W. Sugimura, A. Yamazaki, H. Shigetani, J. Tanaka, and T. Mitsuhashi, *Jpn. J. Appl. Phys.* **36**, 7358 (1997).
- <sup>25</sup>Y. Matsumoto, M. Murakami, Z. Jin, A. Nomura, M. Kawasaki, and H. Koinuma, *SPIE Proc.* **3941**, 19 (2000).
- <sup>26</sup>H. Sakama, G. Osada, M. Tsukamoto, A. Tanokura, and N. Ichikawa, *Thin Solid Films* **515**, 535 (2006).
- <sup>27</sup>M. Murakami, Y. Matsumoto, K. Nakajima, T. Makino, Y. Segawa, T. Chikyow, P. Ahmet, M. Kawasaki, and H. Koinuma, *Appl. Phys. Lett.* **78**, 2664 (2001).
- <sup>28</sup>J. Blomquist, L. E. Walle, P. Uvdal, A. Borg, and A. Sandell, *J. Phys. Chem. C* **112**, 16616 (2008).
- <sup>29</sup>F. Lenzmann, J. Krueger, S. Burnside, K. Brooks, M. Grätzel, D. Gal, S. Rühle, and D. Cahen, *J. Phys. Chem. B* **105**, 6347 (2001).
- <sup>30</sup>D. Vogtenhuber, R. Podloucky, A. Neckel, S. G. Steinemann, and A. J. Freeman, *Phys. Rev. B* **49**, 2099 (1994).
- <sup>31</sup>Y. Nosaka, K. Norimatsu, and H. Miyama, *Chem. Phys. Lett.* **106**, 128 (1984).
- <sup>32</sup>C. J. Howard, T. M. Sabine, and F. Dickson, *Struct. Sci.* **47**, 462 (1991).
- <sup>33</sup>A. G. Thomas, W. R. Flavell, A. R. Kumarasinghe, A. K. Mallick, D. Tsoutsou, G. C. Smith, R. Stockbauer, S. Patel, M. Grätzel, and R. Hengerer, *Phys. Rev. B* **67**, 035110 (2003).
- <sup>34</sup>A. G. Thomas, W. R. Flavell, A. K. Mallick, A. R. Kumarasinghe, D. Tsoutsou, N. Khan, C. Chatwin, S. Rayner, G. C. Smith, R. L. Stockbauer, S. Warren, T. K. Johal, S. Patel, D. Holland, A. Taleb, and F. Wiame, *Phys. Rev. B* **75**, 035105 (2007).
- <sup>35</sup>M. Ramamoorthy, R. D. King-Smith, and D. Vanderbilt, *Phys. Rev. B* **49**, 7709 (1994).
- <sup>36</sup>Z. Zhang, S.-P. Jeng, and V. E. Henrich, *Phys. Rev. B* **43**, 12004 (1991).
- <sup>37</sup>N. Harada, M. Goto, K. Iijima, H. Sakama, N. Ichikawa, H. Kunugita, and K. Ema, *Jpn. J. Appl. Phys.* **46**, 4170 (2007).
- <sup>38</sup>K. Iijima, M. Goto, S. Enomoto, H. Kunugita, K. Ema, M. Tsukamoto, N. Ichikawa, and H. Sakama, *J. Lumin.* **128**, 911 (2008).
- <sup>39</sup>Y. Yamada and Y. Kanemitsu, *Phys. Stat. Solidi C* **8**, 104 (2011).
- <sup>40</sup>A. Furube, T. Asahi, H. Masuhara, H. Yamashita, and M. Anpo, *J. Phys. Chem. B* **103**, 3120 (1999), and references therein.
- <sup>41</sup>H. Zhao, Q. Zhang, and Y. Weng, *J. Phys. Chem. B* **111**, 3762 (2007).
- <sup>42</sup>R. Katoh, M. Murai, and A. Furube, *Chem. Phys. Lett.* **461**, 238 (2008).
- <sup>43</sup>M. Xu, Y. Gao, E. M. Moreno, M. Kunst, M. Muhler, Y. Wang, H. Idriss, and C. Wöll, *Phys. Rev. Lett.* **106**, 138302 (2011).